

## Stellar cores live long and prosper in cuspy dark matter halos

JENNI HÄKKINEN <sup>1</sup>, ALEXANDER RAWLINGS <sup>1</sup>, TILL SAWALA <sup>1</sup> AND MATTHEW G. WALKER <sup>2</sup>

<sup>1</sup>*Department of Physics, University of Helsinki, Gustaf Hällströmin katu 2, FI-00014 Helsinki, Finland*

<sup>2</sup>*McWilliams Center for Cosmology and Astrophysics, Department of Physics, Carnegie Mellon University, Pittsburgh, PA 15213, USA*

### ABSTRACT

The existence of cuspy or cored centers of dark matter halos is a crucial discriminant between different dark matter models. It has recently been claimed based on dynamical arguments that perfectly cored stellar systems cannot survive inside cuspy dark matter halos, which would make the observation of stellar cores in ultra-faint dwarf galaxies, where dark matter cores cannot form through baryonic processes, a direct falsification of the cold dark matter paradigm. Here, we use idealized simulations to show explicitly that cored stellar systems like those observed in dwarf galaxies can be stable within cuspy dark matter halos over at least several Hubble times. We also demonstrate that observations of ultra-faint dwarf galaxies cannot distinguish mildly positive, flat, or negative inner density slopes, further precluding the dynamical inference of the gravitational potential from the stellar configuration.

*Keywords:* Dwarf galaxies (416) — Dwarf spheroidal galaxies (420) — Dark matter (353) — Cold dark matter (265) —  $N$ -body simulations (1083) — Bayesian statistics (1900) — Hierarchical models (1925)

### 1. INTRODUCTION

Dwarf galaxies, and in particular, the dwarf-spheroidal (dSph) and ultra-faint dwarf (UFD) galaxies surrounding the Milky Way, are among the Universe’s most dark-matter-dominated objects. Both in their abundance and in their internal structure, they are key to understanding the nature of dark matter (DM).

In the standard, cold dark matter (CDM) model, collisionless DM forms so-called “cuspy” halos, characterized by a divergent inner density slope that is well described by a Navarro–Frenk–White (NFW) density profile (J. F. Navarro et al. 1997). Observational tests of this prediction on scales of individual galaxies have yielded mixed results. While rotation curves derived for disk galaxies tend to favor “cored” halos of near-uniform density in their central regions (e.g., S.-H. Oh et al. 2011; P. Li et al. 2020), the diversity of observed rotation curves includes individual cases that favor NFW-like cusps (e.g., K. A. Oman et al. 2015).

At the smallest galactic scales, observational tests are further complicated by the fact that the Milky Way’s dSph and UFD satellites are pressure-supported systems, precluding the construction and analysis of rotation curves. Instead, dynamical inferences of their

mass distributions are based on statistical analysis of how member stars populate a 6D phase space that is typically observed in only three dimensions (projected position and line-of-sight velocity).

Various techniques have been used to infer the mass distributions within “classical” dSphs (stellar masses in the range  $\sim 10^4$ – $10^7 M_{\odot}$ ) from photometric, spectroscopic, and in some cases proper motion data — again with mixed results. Several studies conclude that the most luminous dSphs (e.g., Fornax and Sculptor) harbor large DM cores, based on Jeans models (J. I. Read et al. 2019; K. Hayashi et al. 2020), orbit-based Schwarzschild models (J. R. Jardel & K. Gebhardt 2012), direct modeling of the phase-space distribution function (DF) (R. Pascale et al. 2018), and statistical analysis of chemodynamically distinct subpopulations (G. Battaglia et al. 2008; M. G. Walker & J. Peñarrubia 2011; N. C. Amorisco & N. W. Evans 2011; A. Agnello & N. W. Evans 2012). Others, analyzing the same spectroscopic data sets, claim insufficient constraining power to distinguish DM cores from CDM cusps (e.g., L. E. Strigari et al. 2017, 2018; L. Zhu et al. 2016). Including Hubble Space Telescope proper motion data that resolve the internal velocity dispersions of the Draco dSph, E. Vitral et al. (2025) constrain any DM core to have radius  $\lesssim 1$  kpc. Several studies applying homogeneous analyses to all available dSphs conclude that the most luminous ones tend to favor cores, while the least luminous ones favor

cusps (e.g., J. I. Read et al. 2019; K. Hayashi et al. 2020, 2023).

This scenario is consistent with results of some cosmological and hydrodynamical simulations, which show that supernova feedback from sufficiently vigorous star formation can alter the structure of CDM halos, inducing the formation of cores in what would originally have been cuspy halos (J. F. Navarro et al. 1996; S. Mashchenko et al. 2008; A. Pontzen & F. Governato 2012) hosting the most luminous dSphs. This process of astrophysical core formation within CDM halos is expected to become inefficient on scales of the smallest and least luminous UFD galaxies, where feedback from the formation of their paltry stellar populations would have little effect on the structure of the host DM halo (e.g., P. Madau et al. 2014; A. Di Cintio et al. 2014; J. Oñorbe et al. 2015; M. D. A. Orkney et al. 2021).

Thus, the detection of cores in UFDs would directly rule out collisionless CDM. However, the fact that UFDs contain so few stars, usually in a single population, makes the analysis that is already difficult in their brighter counterparts even more so (see, e.g., J. D. Simon 2019, for a review).

In a series of papers, J. Sánchez Almeida et al. (2024a) proposed a new approach to determine the DM density profile of UFDs, requiring only their (projected) surface brightness profiles and applying the Eddington inversion method (J. Sánchez Almeida et al. 2023) to infer the gravitational potential. They concluded that an isotropic stellar population cannot have a cored density profile within a cuspy DM halo, because it implies that the phase-space DF, derived using the Eddington inversion method, has negative values. In particular, J. Sánchez Almeida et al. (2024b) claim that the combined surface brightness profiles of six UFDs require a cored density profile and, thus, rule out a cuspy halo, and J. Sánchez Almeida (2025) explore these in the context of self-interacting DM.

Here, we test this proposition in two parts. Firstly, we explicitly test the stability of cored stellar systems inside cuspy DM halos, using idealized numerical simulations. We find that they can be stable in cuspy halos, provided that the two are initially set up in equilibrium. Secondly, we test the ability to constrain the stellar density profile of UFDs using a finite number of stars. We find that, in particular, the inner slope is degenerate, even before considering observational limitations.

## 2. NUMERICAL METHODS

Traditional cosmological simulations lack both the mass and the spatial resolution to simultaneously model the DM halo and resolve the stellar systems of UFDs.

Furthermore, they require gravitational softening, which could artificially induce or maintain cores in the stellar components (e.g., C. Power et al. 2003).

In this work, we avoid these numerical limitations by representing the DM by an external potential instead of live particles. This allows us to use solar-mass particles and very small softening lengths (1–10 pc, much smaller than the typical core size) for the stellar system. It also greatly reduces the computational cost, allowing us to study a range of parameters and simulate systems over many Hubble times. The choice of an external potential is justified given that the system is completely DM dominated.

### 2.1. Initial conditions

We generate the initial conditions (ICs) used to model the dwarf galaxies using the DF method following M. Hilz et al. (2012). Our fiducial system consists of a stellar component of mass  $M_\star = 5 \times 10^3 M_\odot$  embedded in a DM halo with a virial mass of  $M_{\text{vir}} = 5 \times 10^8 M_\odot$ . The DM component is modeled by an NFW density profile:

$$\rho_{\text{NFW}}(r) = \frac{\rho_{\text{S,NFW}}}{\left(\frac{r}{r_{\text{S,NFW}}}\right) \left[1 + \left(\frac{r}{r_{\text{S,NFW}}}\right)\right]^2}, \quad (1)$$

where the characteristic density  $\rho_{\text{S,NFW}}$  is given by

$$\rho_{\text{S,NFW}} = \frac{M_{\text{vir}}}{4\pi r_{\text{S,NFW}}^3} \times \left[ \log \left( 1 + \frac{r_{\text{vir}}}{r_{\text{S,NFW}}} \right) - \frac{r_{\text{vir}}}{r_{\text{S,NFW}} + r_{\text{vir}}} \right]^{-1}, \quad (2)$$

and the NFW scale radius is given by  $r_{\text{S,NFW}} \equiv r_{\text{vir}}/c$  with a concentration of  $c = 15$ , typical for this halo mass (e.g., B. Diemer & A. V. Kravtsov 2015) in the  $\Lambda$ CDM model. For our fiducial model,  $r_{\text{vir}} \simeq 16.8$  kpc, which corresponds to  $r_{\text{S,NFW}} \simeq 1.12$  kpc.

The stellar component is modeled by a Plummer density profile (J. Binney & S. Tremaine 2008):

$$\rho_{\text{P}}(r) = \frac{3M_\star}{4\pi r_{\text{S,P}}^3} \left[ 1 + \left( \frac{r}{r_{\text{S,P}}} \right)^2 \right]^{-5/2}, \quad (3)$$

where  $r_{\text{S,P}}$  is the Plummer scale radius. Throughout this work, we show results with  $r_{\text{S,P}} = 200$  pc. We also repeated the experiment with  $r_{\text{S,P}} = 50$  pc and found qualitatively identical results.

The DF  $f_i$  is computed for both components from their respective density profiles  $\rho_i$  using Eddington's formula (J. Binney & S. Tremaine 2008):

$$f_i(\mathcal{E}) = \frac{1}{2\sqrt{2}\pi^2} \int_{\Phi_{\text{T}}=0}^{\Phi_{\text{T}}=\mathcal{E}} \frac{d^2\rho_i}{d\Phi_{\text{T}}^2} \frac{d\Phi_{\text{T}}}{\sqrt{\mathcal{E} - \Phi_{\text{T}}}}. \quad (4)$$

Here  $\mathcal{E}$  is the relative energy, and  $\Phi_T$  is the total gravitational potential of the system. We Monte Carlo sample the DF of the stellar component with particles of  $m_\star = 1 M_\odot$ . The radial velocity profiles of the stellar particles are ergodic, and the velocity anisotropy  $\beta_{\text{ani}}$ , defined as

$$\beta_{\text{ani}} \equiv 1 - \frac{\sigma_\theta^2 + \sigma_\phi^2}{2\sigma_r^2}, \quad (5)$$

where  $\sigma_r$ ,  $\sigma_\theta$ , and  $\sigma_\phi$  are the radial, polar, and azimuthal velocity dispersions, respectively, is zero throughout.

## 2.2. Simulations

We run idealized  $N$ -body simulations using the GADGET-4 code (V. Springel et al. 2021), compiled using the Fast Multipole Method with two order multipoles, hierarchical time integration, and an external gravitational field created by a static NFW potential. The stellar distribution is set up to be in equilibrium with the NFW halo at  $t = 0$ . In practice, we add to the equations of motion in GADGET-4 an additional acceleration term due to an external NFW profile of mass  $M_{\text{ext}} = M_{\text{vir}}$ :

$$\begin{aligned} \mathbf{a}_{\text{NFW}} = & \frac{G}{r^3} M_{\text{ext}} \\ & \times \left[ \log \left( 1 + \frac{r}{r_{\text{S,NFW}}} \right) - \frac{r}{r_{\text{S,NFW}}} \left( 1 + \frac{r}{r_{\text{S,NFW}}} \right)^{-1} \right] \\ & \times \left( \log(1+c) - \frac{c}{1+c} \right) \mathbf{x}, \quad (6) \end{aligned}$$

where  $r = |\mathbf{x}|$  as usual.

We create and perform 10 different realizations of our fiducial system. The number of realizations is chosen to mimic the number of UFDs used in the analysis of J. Sánchez Almeida et al. (2024b). To estimate the effect of the external potential, we also deviate its virial mass,  $M_{\text{ext}}$ , (and radius) from that of one of the initial fiducial systems,  $M_{\text{IC}}$ , and perform seven simulations with an unequal mass ratio  $M_{\text{ext}}/M_{\text{IC}}$ . In other words, in these simulations, the initial stellar system is explicitly out of equilibrium with the potential in which it will be evolved.

We investigate the effect of softening by performing simulations with softening lengths of 1, 10 and 100 pc. There was no clear distinction between these values, and we chose a softening of 10 pc to be used for this work.

To study both the short-time evolution and the long-term stability, the simulations are analyzed at  $t = 0$  Gyr, at 100 additional outputs with a cadence of  $\Delta_t = 10$  Myr until  $t = 1$  Gyr, and at 99 additional outputs with a cadence of  $\Delta_t = 1$  Gyr until 100 Gyr.

## 3. EVOLUTION

To calculate the evolution of the stellar density profiles from simulation data, we first center the system using the shrinking-sphere method (C. Power et al. 2003) implemented in PYNBODY (A. Pontzen et al. 2013) and remove the outermost 250 (5%) of stellar particles. In the outskirts of the system, the sampling is poor, and the estimated density can fluctuate significantly, as the random motions of individual particles can cause a net increase of the maximum radii, and hence, an underestimate of the density. We note that in observed UFDs, the outermost 1–10% of stars are also typically not detectable (e.g., H. Richstein et al. 2024) due to the low surface brightness and foreground contamination. We bin the remaining particles in 50 radial shells of equal particle number, each containing 95 particles ( $95 M_\odot$ ). We explicitly test the effect of using different numbers of bins in Appendix A.

Figure 1 shows the evolution of the density and velocity anisotropy profiles of the Plummer stellar system in the external, cuspy gravitational potential. The left column shows the profiles measured from the ICs at  $t = 0$  Gyr and at seven later times up to  $t = 100$  Gyr, for one fiducial system, evolved in the same external potential that was used to generate the ICs. While the density measured in the simulation fluctuates around the Plummer profile from which the ICs were constructed, there is no discernible evolution. In particular, there is no evidence for a change in the inner density profile induced by the evolution in the cuspy gravitational potential.

The right column shows the profiles measured at  $t = 50$  Gyr, in seven simulations which use identical ICs to the one shown on the left but different external potentials. In this case, the density profile can change, with an increased inner stellar density obtained when the external potential is deeper and a lower one when the external potential is shallower than the potential used to generate the ICs. However, provided that the ICs are created in equilibrium with the external potential, the stellar core is maintained.

As noted by J. Sánchez Almeida et al. (2024a), circular orbits ( $\beta_{\text{ani}} \rightarrow -\infty$ ) can accommodate any combination of density and potential, including a cored stellar density in an NFW potential, but those are not physically motivated. Our systems are initially set up with  $\beta_{\text{ani}} = 0$ , and their evolution from this can be seen in the bottom row of Figure 1. As we will show in more detail below, changing the external potential ( $M_{\text{ext}}/M_{\text{IC}} \neq 1$ ) induces net radial motions, which can induce (positive) velocity anisotropy. However, provided that they are evolved in the same potential in which they were cre-

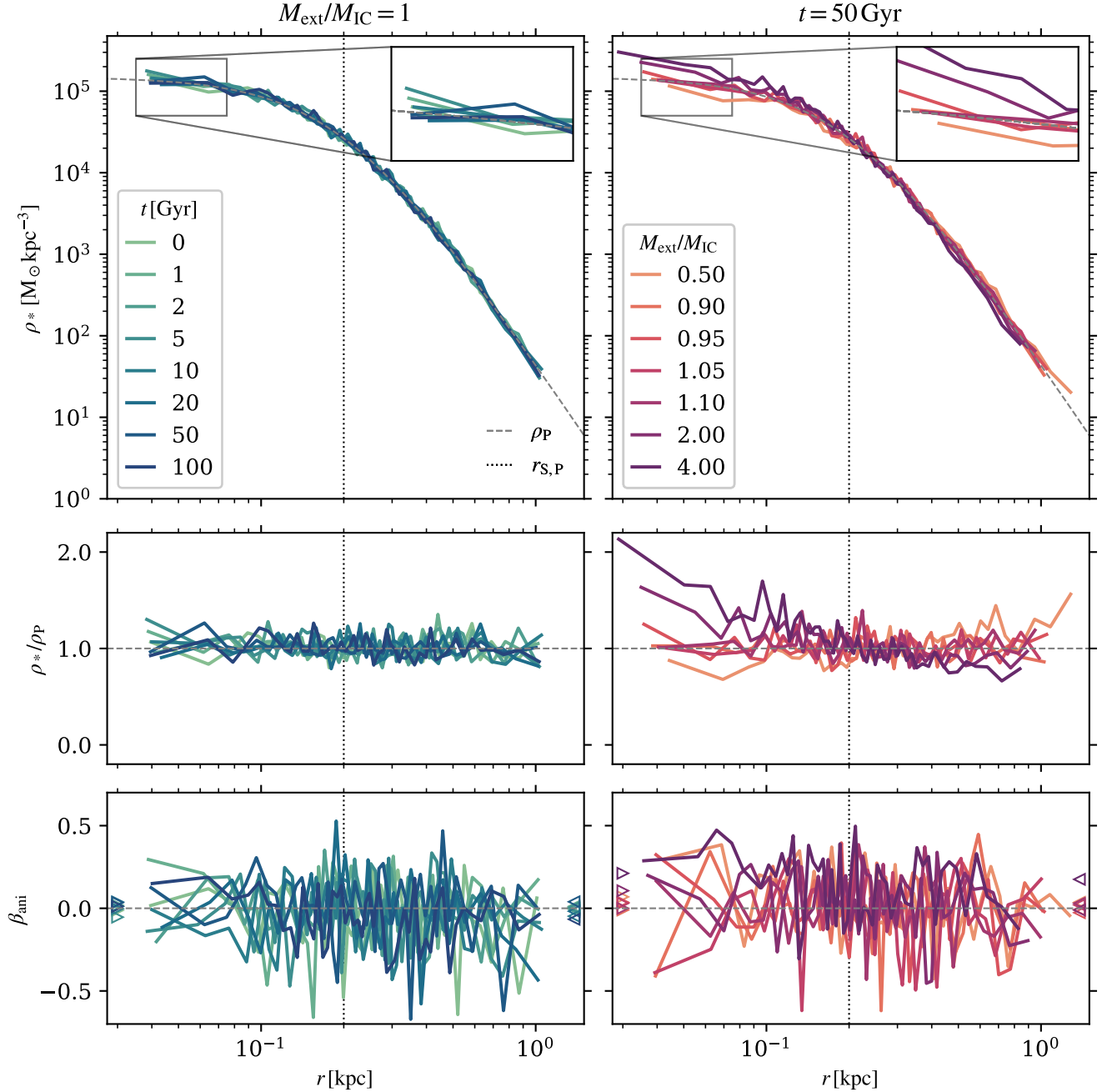


**Figure 1.** Evolution of the stellar density  $\rho_*$  and the velocity anisotropy  $\beta_{\text{ani}}$  in simulations, as a function of radius  $r$ . *Left column:* One realization of the fiducial system for selected times. *Right column:* Seven simulations, where  $M_{\text{ext}}$  is varied from  $M_{\text{IC}}$ , at  $t = 50$  Gyr. *Top row:* Binned  $\rho_*$  from simulation data. The zoomed-in region shows  $\rho_*$  for the inner region within  $r = 0.075$  kpc. The dotted line shows  $r_{\text{S,P}} = 0.2$  kpc, and the dashed line shows the analytic Plummer profile  $\rho_{\text{P}}$ . *Middle row:* The ratio of  $\rho_*$  to  $\rho_{\text{P}}$ , with the dashed line showing  $\rho_*/\rho_{\text{P}} = 1$ . *Bottom row:* Binned  $\beta_{\text{ani}}$  from simulation data, with the dashed line showing  $\beta_{\text{ani}} = 0$ . The triangles show the time-average of  $\beta_{\text{ani}}$  within (on the left) and outside (on the right)  $r_{\text{S,P}}$  for each mass ratio.

ated ( $M_{\text{ext}}/M_{\text{IC}} = 1$ ), our systems maintain isotropy throughout their evolution.

The fluctuations in the density profile shown in Figure 1 arise simply from the fact that the finite number of  $N = 5000$  stars provide only a sample of the underlying

distribution: observations of UFDs, which often contain only of the order of hundreds of stars (e.g., J. D. Simon 2019), are even more susceptible to sampling variance. This effect is demonstrated in Figure 2, which shows the stellar density profiles of 10 different realizations of the

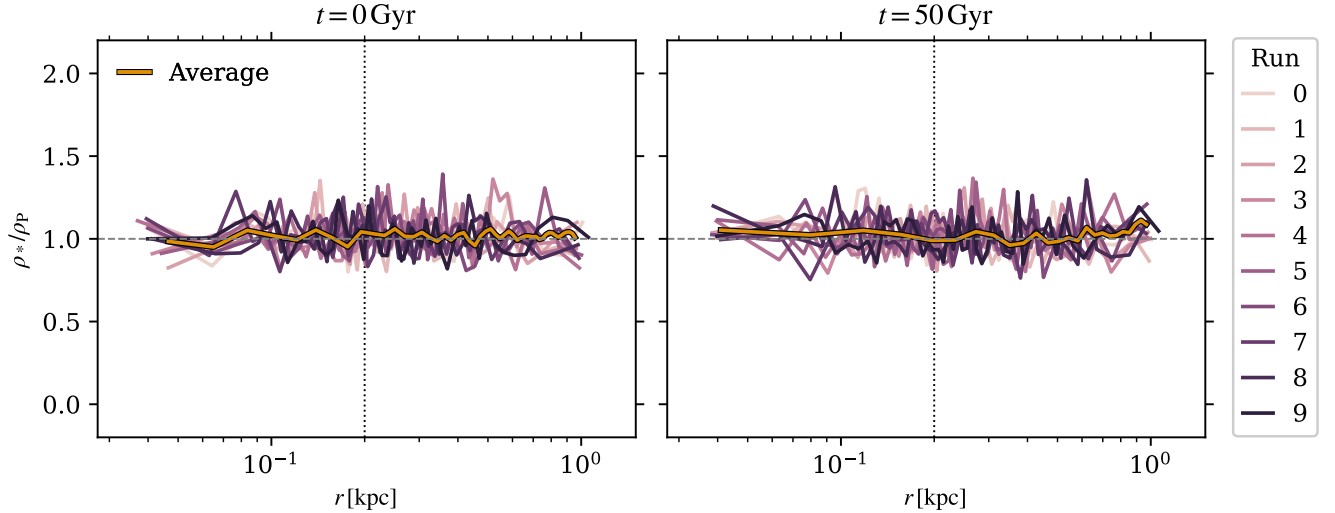


**Figure 2.** Similar to the middle-left panel of Figure 1, but for 10 realizations of the fiducial system, at times  $t = 0$  Gyr (*left*) and  $t = 50$  Gyr (*right*). The orange line shows the average ratio of all 10 runs.

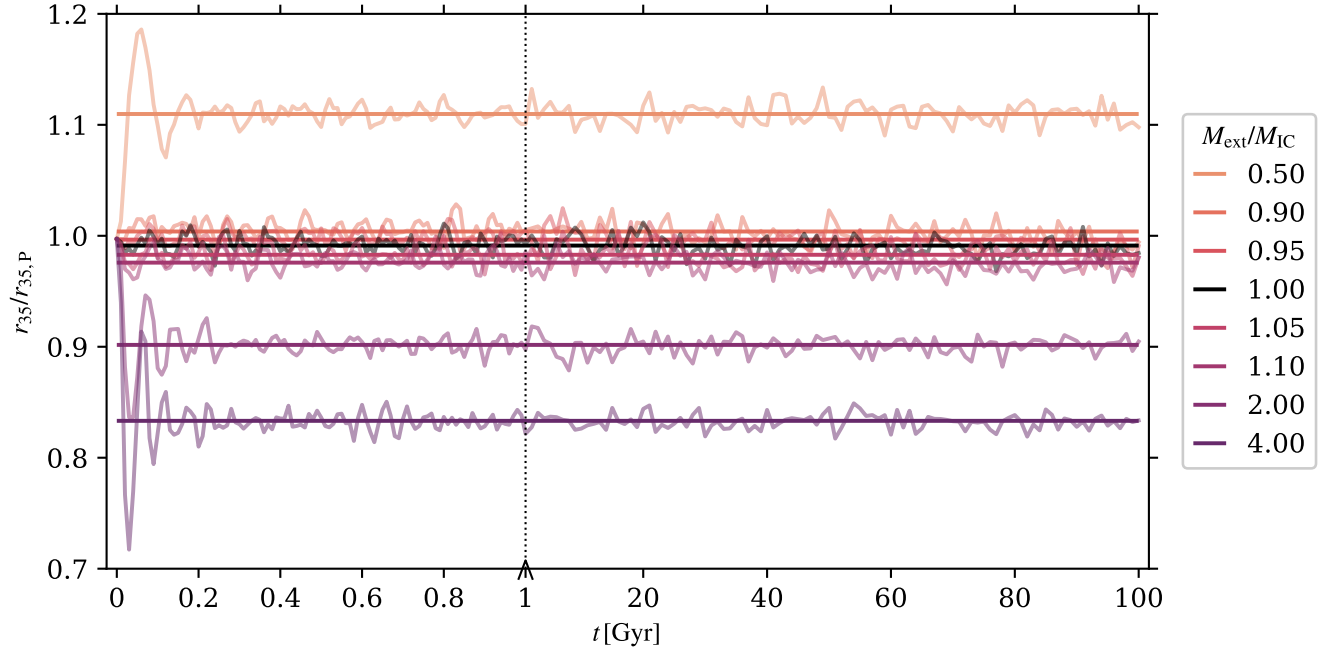


**Figure 3.** The ratio of the Lagrangian radii  $r_{35}$  in simulations to that of the Plummer profile  $r_{35,P}$ , as a function of time  $t$  for eight different mass ratios  $M_{\text{ext}}/M_{\text{IC}}$ . The lighter fluctuating lines show the evolution at each output, while the darker horizontal lines corresponds to the time-averaged value across the whole simulation. The  $t$ -axis is divided into two ranges separated by the black dotted line: the left side shows the evolution within the first 1 Gyr and the right side within the remaining 99 Gyr.

fiducial system, both in the ICs and at  $t = 50$  Gyr. Each individual profile fluctuates around the Plummer value, with  $\rho_*/\rho_P \sim 10\%$ . The average of all 10 realizations is close to the Plummer value. There is no discernible evolution, neither in the average nor in any of the individual profiles.

A more fine-grained view of the evolution is shown in Figure 3, which compares the radius that encloses 35% of stellar particles,  $r_{35}$ , in simulations to that of the analytic Plummer profile,  $r_{35,P}$ , which is approximately equal to the scale radius of the ICs ( $r_{S,P} = 0.2$  kpc). The simulations shown here are the same ones as in Figure 1.

It can be seen that evolving the stellar distribution in an external potential much shallower than that used to create the ICs leads to a rapid expansion of the core, followed by a damped oscillation, before a new equilibrium is obtained in a more extended stellar system. Conversely, an external potential much deeper than that used to create the ICs leads to a rapid collapse, a damped oscillation, and finally a more compact stellar system. In each case, the new equilibrium is reached in less than 200 Myr.

Due to the finite sampling, random fluctuations in  $r_{35}$  persist throughout the remaining 100 Gyr, making the evolution of systems with small changes to the external potential difficult to distinguish. For this reason, we also show the time-averaged values of  $r_{35}$ , which demonstrate these differences better. The time-averaged value of the fiducial system ( $M_{\text{ext}}/M_{\text{IC}} = 1$ ) is very slightly below  $r_{35}/r_{35,P} = 1$ , which can be considered to be caused by sample variance.

In summary, while stellar systems do respond to changes in the external potential, stellar cores can be maintained within cuspy DM halos for many Hubble times.

#### 4. STELLAR DENSITY INFERENCE

Having demonstrated that cored stellar systems can, in fact, be stable and long-lived in cuspy DM halos, we will revisit the previous research which had suggested the opposite conclusion.

We note that a crucial assertion when applying the Eddington inversion method to rule out cuspy DM halos is the presence of stellar cores, and more specifically, the presence of non-negative inner density slopes. In [J. Sánchez Almeida et al. \(2024b\)](#), this assertion is supported by fitting a 5<sup>th</sup>-order polynomial to the combined projected surface density profiles of six UFDs from [H. Richstein et al. \(2024\)](#). Here, we test the ability to distinguish different inner density slopes with our simulated stellar Plummer profiles in the fiducial setup ( $M_{\text{ext}} = M_{\text{IC}}$ ).

We fit at times  $t = (0, 1, 2, 5, 10, 20, 50, 100)$  Gyr the full 3D information of the stellar distribution with the  $(\alpha, \beta, \gamma)$  double power-law profile ([D. Merritt et al. 2006](#); [A. Di Cintio et al. 2014](#)):

$$\rho(r) = \frac{\rho_S}{\left(\frac{r}{r_S}\right)^\gamma \left[1 + \left(\frac{r}{r_S}\right)^\alpha\right]^{\alpha(\beta-\gamma)/\alpha}}. \quad (7)$$

Here  $\rho_S$  is a characteristic density and  $r_S$  a characteristic scale length. The inner and outer regions have logarithmic slopes of  $-\gamma$  and  $-\beta$ , respectively, with the transition between these regions governed by  $\alpha$ . A Plummer sphere ([Equation 3](#)) has  $(\alpha, \beta, \gamma) = (2, 5, 0)$ , whereas for

an NFW profile ([Equation 1](#)), the parameterization is  $(1, 3, 1)$ .

To infer the analytic stellar density profile from the simulation data, we fit the  $(\alpha, \beta, \gamma)$  profile to the stellar density, using the same binning as discussed in [section 3](#).

We use hierarchical Bayesian inference to jointly fit the density profiles of all 10 fiducial runs at the aforementioned times: a detailed methodology is provided in [Appendix B](#). This way, we avoid many of the problems — such as overfitting, loss of data heterogeneity, and diminished precision of parameter estimates for small sample sizes — that are commonly associated with inference performed when completely stacking the data into a single set or performing inference on related datasets independently ([A. Gelman & J. Hill 2006](#)).

An important finding of our analysis is the inability to constrain  $\gamma$  as strictly-positive at any time, indicating that despite *a priori* knowledge that the derivative of the stellar density profile from which our samples are drawn is always  $d\rho/dr \leq 0$ , this cannot be unequivocally said from the measured density profile. By maximizing the data available in the inference, we constrain the population mean and standard deviation of the inner density slope at  $t = 0$  Gyr as  $\mu_\gamma = -0.005_{-0.208}^{+0.178}$  and  $\sigma_\gamma = 0.011_{-0.010}^{+0.026}$ , respectively, where the uncertainties refer to the 90% confidence interval of the parameter. The time evolution of the full distribution of  $\gamma$  is shown in the top-left panel of [Figure 4](#). At all times,  $\gamma$  is consistent with a value of 0, however the spread in the distributions means that  $\gamma < 0$  could be easily inferred: we find that the probability  $P(\gamma \leq 0) = 0.52$ .

For comparison, we fit a non-hierarchical model independently to the 10 fiducial simulations at  $t = 0$  Gyr (i.e., we fit for the parameters in the  $(\alpha, \beta, \gamma)$  profile directly). Unsurprisingly, the constraints on  $\gamma$  are significantly weaker when inferring the density model parameters independently for each simulation compared to the partial-stacking allowed for by the hierarchical model, as shown in the top-right panel of [Figure 4](#). While all individual realizations are drawn from the same underlying Plummer distribution with  $\gamma = 0$ , due to sample variance, the probability distribution function (PDF) inferred from each realization differs. In particular, in every realization, the PDF extends to both positive and negative values of  $\gamma$ .

To demonstrate degeneracies between the parameters of the fitted  $(\alpha, \beta, \gamma)$  profile, in the bottom panels of [Figure 4](#) we show contours of the 68% and 95% confidence intervals of the inferred parameters for the hierarchical model. We see that their true values ( $\alpha = 2$ ,  $\beta = 5$ ,  $\gamma = 0$ ,  $r_S = 0.2$  kpc, and  $\rho_S \simeq 1.5 \times 10^5 M_\odot \text{kpc}^{-3}$ ) are recovered very well in this case. However,  $\gamma$  is strongly

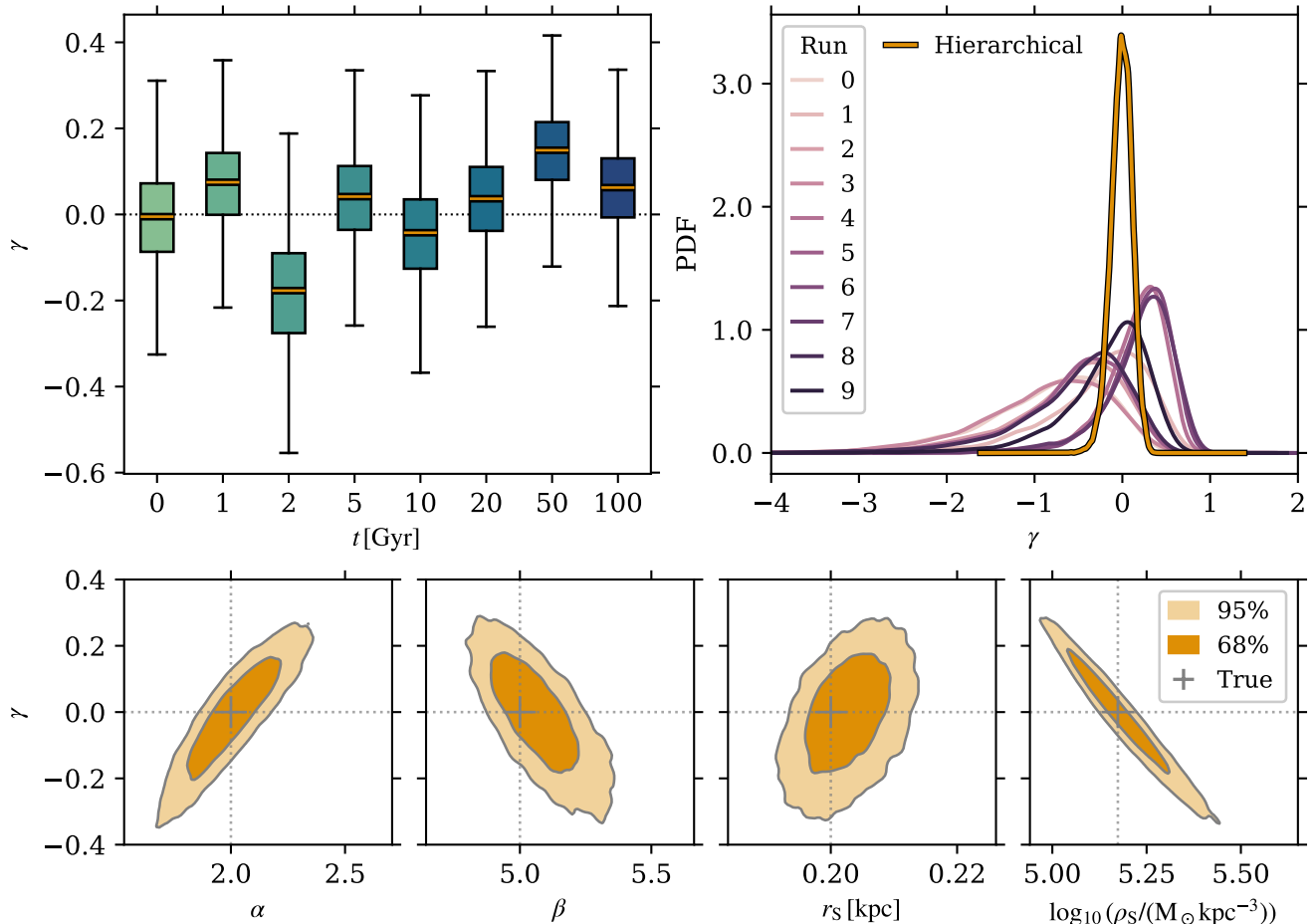


**Figure 4.** Results of the stellar density fitting. *Top-left panel:* The distribution of  $\gamma$  for selected times (same as in the left column of Figure 1) for the hierarchical fit. The orange lines show the median of the fit at each time, and the dotted line shows  $\gamma = 0$ . *Top-right panel:* The PDF of  $\gamma$  at  $t = 0$  Gyr. The orange line shows the hierarchical fit, and the remaining lines the non-hierarchical fits for the 10 fiducial simulations. *Bottom panels:* Correlation of  $\gamma$  with the parameters  $\alpha$ ,  $\beta$ ,  $r_s$ , and  $\rho_s$ , respectively. The contours show their 68% and 95% confidence intervals, and the dashed crossing lines show the true parameters of the underlying Plummer distribution.

correlated with the other parameters, especially with  $\rho_s$  but also clearly with  $\alpha$  and  $\beta$ .

## 5. DISCUSSION

When we discuss cores, we use the widely adopted definition of density profiles that are asymptotically flat, i.e., whose inner slope  $d\rho/dr \rightarrow 0$  as  $r \rightarrow 0$ . That is, we consider a density profile such as the Plummer profile (Equation 3), or the  $(\alpha, \beta, \gamma)$  profile (Equation 7) with  $\gamma = 0$ , to be cored, even though  $d\rho/dr < 0$  for any finite  $r$ . Applying the Eddington inversion method to rule out cuspy potentials may require a more limited definition ( $d\rho/dr > 0$  at some finite radius) by which Plummer profiles would not be considered cored. However, we have shown that for typical UDFs, measurements of the true inner slope from small numbers of stars are ambiguous.

A known constraint of the Eddington inversion method (J. Sánchez Almeida et al. 2024a) is that perfect stellar cores with  $\gamma \leq 0$  are incompatible with NFW potentials when the velocity distribution is isotropic or radially biased ( $\beta_{\text{ani}} \geq 0$ ). The incompatibility arises from the method producing a DF that is not everywhere non-negative (i.e., there exists an  $\mathcal{E}$  such that  $f(\mathcal{E}) < 0$ ), and is hence unphysical.

If we consider our ICs, which are by definition ergodic and spherically-symmetric, the DF is solely a function of the relative energy (as in Equation 4). Effectively,  $f$  tells us the probability of finding a stellar particle in the system with an energy in the infinitesimal volume  $d\mathcal{E}$  about  $\mathcal{E}$ . In practice however, we are unable to numerically sample from such an infinitesimal volume, and rather sample from a *coarsened* DF  $\bar{f}(\mathcal{E})$  (J. Binney & S. Tremaine 2008) that defines a finite volume of width

$\Delta\mathcal{E}$ , where  $\bar{f}$  is the expectation value, or mean, of  $f$  within the volume  $\Delta\mathcal{E}$ . Critically, whilst  $\bar{f}(\mathcal{E})$  may be everywhere non-negative in the volume  $\Delta\mathcal{E}$ ,  $f(\mathcal{E})$  in a subregion  $d\mathcal{E} \in \Delta\mathcal{E}$  may not be. The task then becomes ensuring that our approximation

$$\lim_{N \rightarrow \infty} \sum_i^N \bar{f}(\mathcal{E}_i) \rightarrow \int_{\Omega} f(\mathcal{E}) d\mathcal{E} \quad (8)$$

is a good one over the domain  $\Omega$ .

In creating our ICs, we calculate  $f$  at  $2 \times 10^3$  equally-spaced values of  $\mathcal{E}$ : this defines our coarsened DF<sup>3</sup>. We have tested the effect of increasing the number of  $\mathcal{E}$  values  $f$  is evaluated at by a factor of 10, and performed a two-sample Kolmogorov–Smirnov (KS) test with a two-tailed null hypothesis to assess if there is a meaningful difference between evaluations of the DF. We find that the test statistic is  $t_{\text{KS}} = 9.5 \times 10^{-4}$  and the  $p$ -value is  $\sim 1.0$ : the DFs are indistinguishable. Consequently, we are confident that our constructed  $\bar{f}$  is a good approximation to the true  $f$ . This is further supported by the constructed ICs agreeing well with the desired Plummer profile (shown in Figure 4). While negative DFs are clearly unphysical, analytic DFs are only descriptive, which real and finite systems are not required to fully sample.

## 6. CONCLUSIONS

The existence of cored rather than cuspy DM profiles in UFDs would have profound implications, effectively falsifying the standard cosmological model. However, our results challenge previous assertions of evidence for DM cores based on cored stellar density profiles. Firstly, we have shown that cored stellar systems can persist within cuspy halos, provided that they have formed in initial equilibrium, as would be expected for a stellar system forming within an existing DM halo in the standard galaxy formation paradigm.

Secondly, we have demonstrated the limitations of determining the crucial inner slope of the stellar density profiles of UFDs. Even with a conservative sample size

and in the absence of observational errors, it is exceptionally difficult to distinguish in UFDs a mildly positive, negative, or zero inner density gradient. This is heightened by the small collection of stars that constitute such a dwarf galaxy, increasing the observed variance in stellar mass density profiles. While future observations may yet lead to a viable application of the Eddington inversion method, we conclude that based on current observations, the existence of stellar cores in UFDs provides no evidence against cuspy DM halos.

## ACKNOWLEDGMENTS

J.H. acknowledges the support of the Magnus Ehrnrooth Foundation. A.R. acknowledges the support of the University of Helsinki Research Foundation. J.H. and T.S. acknowledge support by Research Council of Finland grants 354905 and 339127. J.H., A.R., and T.S. acknowledge support by ERC Consolidator Grant KETJU (no. 818930). M.G.W. acknowledges support from the National Science Foundation (NSF) grant AST-2206046. This work used facilities hosted by the CSC – IT Centre for Science, Finland.

## AUTHOR CONTRIBUTIONS

**JH**: data curation, formal analysis, investigation, methodology, visualization, writing – original draft. **AR**: formal analysis, investigation, methodology, software, writing – original draft. **TS**: conceptualization, supervision, writing – original draft. **MGW**: conceptualization, writing – original draft.

*Software*: GADGET-4 (V. Springel et al. 2021), PYNBODY (A. Pontzen et al. 2013), NumPy (C. R. Harris et al. 2020), SciPy (P. Virtanen et al. 2020), Matplotlib (J. D. Hunter 2007), STAN (Stan Development Team 2018), CmdStanPy (Stan Development Team 2018), Arviz (R. Kumar et al. 2019).

## APPENDIX

### A. BINNING OF STELLAR PARTICLES

We test the effect of using different numbers of bins when constructing radial profiles on our conclusions, in particular for the inference of the  $(\alpha, \beta, \gamma)$  double power-law profile. In all cases, we use bins of equal particle counts (as opposed to equal bin widths) to ensure sufficient and comparable sample sizes within each bin from which we determine

<sup>3</sup> Note that we use interpolation so as to evaluate our DF at any  $\mathcal{E}$ , and not just at the values used to construct the DF.

**Table 1.** Weakly informative prior distributions for the  $(\alpha, \beta, \gamma)$  double power-law density profile. The parameter distributions refer to the single-line circle node variables in Figure 5.

Hyperparameter	Distribution	Truncation
$\mu_{\log_{10} \rho_S}$	$\mathcal{N}(5, 1)$	$-5 \leq x \leq 10$
$\sigma_{\log_{10} \rho_S}$	$\mathcal{N}(0, 1)$	$x > 0$
$\mu_{\log_{10} r_S}$	$\mathcal{N}(0, 1)$	None
$\sigma_{\log_{10} r_S}$	$\mathcal{N}(0, 0.5)$	$x > 0$
$\mu_{\log_{10} \alpha}$	$\mathcal{N}(0, 0.5)$	None
$\sigma_{\log_{10} \alpha}$	$\mathcal{N}(0, 0.5)$	$x > 0$
$\mu_\beta$	$\mathcal{N}(0, 4)$	None
$\sigma_\beta$	$\mathcal{N}(0, 2)$	$x > 0$
$\mu_\gamma$	$\mathcal{N}(0, 2)$	None
$\sigma_\gamma$	$\mathcal{N}(0, 2)$	$x > 0$
$\tau$	$\mathcal{N}(0, 1)$	$x > 0$
$L_c$	LKJCholesky(2)	None
$z$	$\mathcal{N}(0, 1)$	None

statistics, such as the mean density within a bin. In the following, we discuss signal-to-noise (S/N) in the Poisson sense, i.e.,  $S/N = N/\sqrt{N} = \sqrt{N}$ .

We first note that determining an optimal binning strategy is a result of two competing factors (e.g., Y. Tarumi et al. 2021): increasing S/N, achieved with increasing the number of particles per bin, and increasing spatial resolution, achieved with increasing the total number of bins. Motivated by observational campaigns of UFDs (e.g., A. Drlica-Wagner et al. 2015; C. Y. Tan et al. 2025), we require that the minimum S/N in each radial bin is  $S/N \simeq 10 \implies N \simeq 100$ . We thus try binning the inner 95% of stellar particles using 5, 10, 25, and 50 bins of equal particle counts<sup>4</sup>. Already we note that using 5 bins, whilst achieving a high S/N of  $\sim 30$ , barely resolves the inner regions of the stellar profile  $r < r_S$ , thus setting a lower limit to the number of bins. Using 50 bins achieves our desired  $S/N \simeq 10$ , thus setting our upper limit.

For each binning strategy, we attempt to infer the parameters  $\alpha$ ,  $\beta$ ,  $\gamma$ , and  $r_S$  of the double-power law model from our ICs (see Appendix B), which we know *a priori* to be 2, 5, 0, and 0.2, respectively. We then determine the Mahalanobis distance between the posterior median of the parameters and the known values: unlike the Euclidean measure, the Mahalanobis measure accounts for the covariance  $V$  between the parameters. The Mahalanobis distance is defined as

$$d_M = \sqrt{(\theta_{\text{posterior}} - \theta_{\text{true}})^T V^{-1} (\theta_{\text{posterior}} - \theta_{\text{true}})}. \quad (\text{A1})$$

A smaller  $d_M$  is indicative of a better recovery of the *a priori* truth than a higher  $d_M$ . We find that as a function of bin count,  $d_M$  decreases exponentially as  $d_M \propto N_{\text{bin}}^{-0.43}$ : from  $N_{\text{bin}} = 25$  to  $N_{\text{bin}} = 50$ , the difference in distance measures is only  $\Delta d_M = 0.24$ , indicating the two strategies recover the *a priori* truth comparatively well. We thus adopt the binning that provides the higher spatial resolution, namely  $N_{\text{bin}} = 50$ , as the chosen binning strategy in this work.

## B. FITTING DENSITY PROFILES

We fit the  $(\alpha, \beta, \gamma)$  double power-law profile using hierarchical Bayesian inference implemented in STAN (Stan Development Team 2018), with four chains of 2000 posterior draws each (i.e., post burn-in period). Recognizing that the 10 fiducial simulations describe the same physical system, albeit with different realizations of the particle sampling, we can jointly model the individual density profile parameters, denoted  $\theta \equiv [\log_{10} \rho_S, \log_{10} r_S, \log_{10} \alpha, \beta, \gamma]$ , as realizations of a *population* of possible density profiles that satisfy the exchangeability criterion (A. Gelman et al. 2015). The population distribution of density profiles is governed by hyperparameters on each of the latent (or observed) parameters in  $\theta$  that themselves have weakly-informative priors. The prior distributions for the hyperparameters are given in Table 1, and a graphical representation of the Bayesian model in the form of a directed acyclic graph is given in Figure 5. Each latent parameter in  $\theta$  we assign a normal distribution, with mean  $\mu_X$  and standard deviation  $\sigma_X$  for

<sup>4</sup> We also tested a case using 95 bins, however due to the low S/N the profile fits were unable to be recovered.

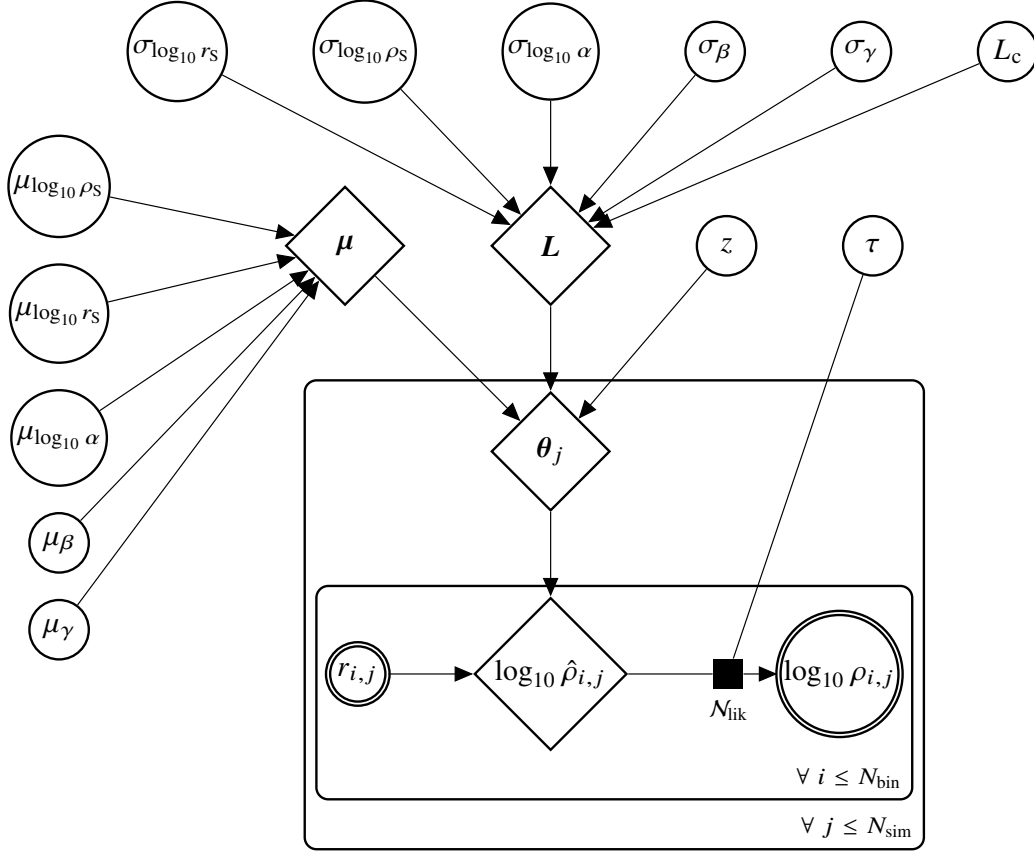


**Figure 5.** Directed acyclic graph showing the model parameters in the fit to the density profile. Single-line circle nodes represent fit parameters, double-line circles represent measured quantities (the data), and diamond nodes represent deterministic quantities. Parameters outside the inner rectangle do not depend on the measured radius.

the respective variable  $X \in \boldsymbol{\theta}$ . To capture any covariance between latent parameters, we directly model the correlation matrix  $\Omega = L_c L_c^\top$ , where  $L_c$  is the Cholesky factor<sup>5</sup> of the correlation matrix. We assign a [D. Lewandowski et al. \(2009\)](#) prior on  $L_c$  as  $L_c \sim \text{LKJCholesky}(\eta)$ , with the prior on the correlation matrix thus becoming  $p(\Omega|\eta) \propto \det(\Omega)^{\eta-1}$ . The variable  $\eta$  controls the concentration of the prior about the identity matrix: by setting  $\eta = 2$  ([Table 1](#)), we mildly-favor weak correlations while allowing moderate correlation structure.

We define two new vectors of parameters:

$$\boldsymbol{\mu} = [\mu_{\log_{10} \rho_S}, \mu_{\log_{10} r_S}, \mu_{\log_{10} \alpha}, \mu_\beta, \mu_\gamma] \quad (\text{B2})$$

$$\mathbf{L} = \text{diag} [\sigma_{\log_{10} \rho_S}, \sigma_{\log_{10} r_S}, \sigma_{\log_{10} \alpha}, \sigma_\beta, \sigma_\gamma] \cdot L_c, \quad (\text{B3})$$

from which the latent parameter vector  $\boldsymbol{\theta}$  is determined as

$$\boldsymbol{\theta} = \mathbf{1} \cdot \boldsymbol{\mu}^\top + \mathbf{L}z. \quad (\text{B4})$$

After the posterior sampling, we perform standard convergence and posterior-predictive checks to ensure the fits are robust by enforcing a diagnostic value  $\hat{R}$  (comparison of between-chain and within-chain variance) of less than 1.05, a high effective sample, and that the number of divergent transitions is less than 1 percent (for details, see [A. Vehtari et al. 2021](#); [Stan Development Team 2018](#)). We perform an additional prior sensitivity analysis using the power-scaling method described in [N. Kallioinen et al. \(2024\)](#), ensuring that the sensitivity diagnostic is less than 0.05 for the latent

<sup>5</sup> The Cholesky factor of a positive-definite matrix is a lower-triangular matrix  $L$  such that  $\Sigma = LL^\top$ .

parameters  $\theta$  of the model. In doing so, we quantitatively ensure that the obtained posterior distributions are not strongly-dependent on the assumed prior distributions.

As our model takes a number of free parameters, degeneracies between parameters are possible, thus highlighting the importance of using a Bayesian method to propagate parameter uncertainty. Typically, we find that the inner slope  $\gamma$  is strongly negatively-correlated with the characteristic density  $\log_{10} \rho_S$ , as well as being correlated to a lesser degree with both  $\alpha$  (positively) and  $\beta$  (negatively). Consequently,  $\log_{10} \rho_S$  tends to be negatively-correlated with  $\alpha$  and positively-correlated with  $\beta$ .

## REFERENCES

- Agnello, A., & Evans, N. W. 2012, *The Astrophysical Journal*, 754, L39, doi: [10.1088/2041-8205/754/2/L39](https://doi.org/10.1088/2041-8205/754/2/L39)
- Amorisco, N. C., & Evans, N. W. 2011, *MNRAS*, 411, 2118, doi: [10.1111/j.1365-2966.2010.17715.x](https://doi.org/10.1111/j.1365-2966.2010.17715.x)
- Battaglia, G., Helmi, A., Tolstoy, E., et al. 2008, *ApJL*, 681, L13, doi: [10.1086/590179](https://doi.org/10.1086/590179)
- Binney, J., & Tremaine, S. 2008, *Galactic Dynamics: Second Edition* (Princeton University Press)
- Di Cintio, A., Brook, C. B., Dutton, A. A., et al. 2014, *MNRAS*, 441, 2986, doi: [10.1093/mnras/stu729](https://doi.org/10.1093/mnras/stu729)
- Diemer, B., & Kravtsov, A. V. 2015, *ApJ*, 799, 108, doi: [10.1088/0004-637X/799/1/108](https://doi.org/10.1088/0004-637X/799/1/108)
- Drlica-Wagner, A., Bechtol, K., Rykoff, E. S., et al. 2015, *ApJ*, 813, 109, doi: [10.1088/0004-637X/813/2/109](https://doi.org/10.1088/0004-637X/813/2/109)
- Gelman, A., Carlin, J. B., Stern, H. S., et al. 2015, *Bayesian Data Analysis*, 3rd edn. (Chapman and Hall/CRC)
- Gelman, A., & Hill, J. 2006, *Data Analysis Using Regression and Multilevel/Hierarchical Models*, Analytical Methods for Social Research (Cambridge University Press)
- Harris, C. R., Millman, K. J., van der Walt, S. J., et al. 2020, *Nature*, 585, 357, doi: [10.1038/s41586-020-2649-2](https://doi.org/10.1038/s41586-020-2649-2)
- Hayashi, K., Chiba, M., & Ishiyama, T. 2020, *ApJ*, 904, 45, doi: [10.3847/1538-4357/abbe0a](https://doi.org/10.3847/1538-4357/abbe0a)
- Hayashi, K., Hirai, Y., Chiba, M., & Ishiyama, T. 2023, *ApJ*, 953, 185, doi: [10.3847/1538-4357/ace33e](https://doi.org/10.3847/1538-4357/ace33e)
- Hilz, M., Naab, T., Ostriker, J. P., et al. 2012, *MNRAS*, 425, 3119, doi: [10.1111/j.1365-2966.2012.21541.x](https://doi.org/10.1111/j.1365-2966.2012.21541.x)
- Hunter, J. D. 2007, *Computing in Science & Engineering*, 9, 90, doi: [10.1109/MCSE.2007.55](https://doi.org/10.1109/MCSE.2007.55)
- Jardel, J. R., & Gebhardt, K. 2012, *The Astrophysical Journal*, 746, 89, doi: [10.1088/0004-637x/746/1/89](https://doi.org/10.1088/0004-637x/746/1/89)
- Kallioinen, N., Paananen, T., Bürkner, P.-C., & Vehtari, A. 2024, *Statistics and Computing*, 34, 57, doi: [10.1007/s11222-023-10366-5](https://doi.org/10.1007/s11222-023-10366-5)
- Kumar, R., Carroll, C., Hartikainen, A., & Martin, O. 2019, *Journal of Open Source Software*, 4, 1143, doi: [10.21105/joss.01143](https://doi.org/10.21105/joss.01143)
- Lewandowski, D., Kurowicka, D., & Joe, H. 2009, *Journal of Multivariate Analysis*, 100, 1989, doi: [None](https://doi.org/10.1016/j.jmva.2009.04.001)
- Li, P., Lelli, F., McGaugh, S., & Schombert, J. 2020, *ApJS*, 247, 31, doi: [10.3847/1538-4365/ab700e](https://doi.org/10.3847/1538-4365/ab700e)
- Madau, P., Shen, S., & Governato, F. 2014, *ApJL*, 789, L17, doi: [10.1088/2041-8205/789/1/L17](https://doi.org/10.1088/2041-8205/789/1/L17)
- Mashchenko, S., Wadsley, J., & Couchman, H. M. P. 2008, *Science*, 319, 174, doi: [10.1126/science.1148666](https://doi.org/10.1126/science.1148666)
- Merritt, D., Graham, A. W., Moore, B., Diemand, J., & Terzić, B. 2006, *AJ*, 132, 2685, doi: [10.1086/508988](https://doi.org/10.1086/508988)
- Navarro, J. F., Eke, V. R., & Frenk, C. S. 1996, *MNRAS*, 283, L72, doi: [10.1093/mnras/283.3.L72](https://doi.org/10.1093/mnras/283.3.L72)
- Navarro, J. F., Frenk, C. S., & White, S. D. M. 1997, *ApJ*, 490, 493, doi: [10.1086/304888](https://doi.org/10.1086/304888)
- Oñorbe, J., Boylan-Kolchin, M., Bullock, J. S., et al. 2015, *MNRAS*, 454, 2092, doi: [10.1093/mnras/stv2072](https://doi.org/10.1093/mnras/stv2072)
- Oh, S.-H., de Blok, W. J. G., Brinks, E., Walter, F., & Kennicutt, Jr., R. C. 2011, *AJ*, 141, 193, doi: [10.1088/0004-6256/141/6/193](https://doi.org/10.1088/0004-6256/141/6/193)
- Oman, K. A., Navarro, J. F., Fattahi, A., et al. 2015, *MNRAS*, 452, 3650, doi: [10.1093/mnras/stv1504](https://doi.org/10.1093/mnras/stv1504)
- Orkney, M. D. A., Read, J. I., Rey, M. P., et al. 2021, *MNRAS*, 504, 3509, doi: [10.1093/mnras/stab1066](https://doi.org/10.1093/mnras/stab1066)
- Pascale, R., Posti, L., Nipoti, C., & Binney, J. 2018, *MNRAS*, 480, 927, doi: [10.1093/mnras/sty1860](https://doi.org/10.1093/mnras/sty1860)
- Pontzen, A., & Governato, F. 2012, *MNRAS*, 421, 3464, doi: [10.1111/j.1365-2966.2012.20571.x](https://doi.org/10.1111/j.1365-2966.2012.20571.x)
- Pontzen, A., Roškar, R., Stinson, G. S., et al. 2013, *pynbody: Astrophysics Simulation Analysis for Python*
- Power, C., Navarro, J. F., Jenkins, A., et al. 2003, *MNRAS*, 338, 14, doi: [10.1046/j.1365-8711.2003.05925.x](https://doi.org/10.1046/j.1365-8711.2003.05925.x)
- Read, J. I., Walker, M. G., & Steger, P. 2019, *MNRAS*, 484, 1401, doi: [10.1093/mnras/sty3404](https://doi.org/10.1093/mnras/sty3404)
- Richstein, H., Kallivayalil, N., Simon, J. D., et al. 2024, *ApJ*, 967, 72, doi: [10.3847/1538-4357/ad393c](https://doi.org/10.3847/1538-4357/ad393c)
- Sánchez Almeida, J. 2025, *arXiv e-prints*, arXiv:2510.05682. <https://arxiv.org/abs/2510.05682>
- Sánchez Almeida, J., Plastino, A. R., & Trujillo, I. 2023, *ApJ*, 954, 153, doi: [10.3847/1538-4357/ace534](https://doi.org/10.3847/1538-4357/ace534)
- Sánchez Almeida, J., Plastino, A. R., & Trujillo, I. 2024a, *Astron. Astrophys.*, 690, A151, doi: [10.1051/0004-6361/202449187](https://doi.org/10.1051/0004-6361/202449187)

- Sánchez Almeida, J., Trujillo, I., & Plastino, A. R. 2024b, *Astrophys. J. Lett.*, 973, L15, doi: [10.3847/2041-8213/ad66bc](https://doi.org/10.3847/2041-8213/ad66bc)
- Simon, J. D. 2019, *ARA&A*, 57, 375, doi: [10.1146/annurev-astro-091918-104453](https://doi.org/10.1146/annurev-astro-091918-104453)
- Springel, V., Pakmor, R., Zier, O., & Reinecke, M. 2021, *Monthly Notices of the Royal Astronomical Society*, 506, 2871, doi: [10.1093/mnras/stab1855](https://doi.org/10.1093/mnras/stab1855)
- Stan Development Team. 2018, The Stan Core Library, <http://mc-stan.org>
- Strigari, L. E., Frenk, C. S., & White, S. D. M. 2017, *The Astrophysical Journal*, 838, 123, doi: [10.3847/1538-4357/aa5c8e](https://doi.org/10.3847/1538-4357/aa5c8e)
- Strigari, L. E., Frenk, C. S., & White, S. D. M. 2018, *The Astrophysical Journal*, 860, 56, doi: [10.3847/1538-4357/aac2d3](https://doi.org/10.3847/1538-4357/aac2d3)
- Tan, C. Y., Cerny, W., Drlica-Wagner, A., et al. 2025, *ApJ*, 979, 176, doi: [10.3847/1538-4357/ad9b0c](https://doi.org/10.3847/1538-4357/ad9b0c)
- Tarumi, Y., Suda, T., van de Voort, F., et al. 2021, *MNRAS*, 505, 3755, doi: [10.1093/mnras/stab1487](https://doi.org/10.1093/mnras/stab1487)
- Vehtari, A., Gelman, A., Simpson, D., Carpenter, B., & Bürkner, P.-C. 2021, *Bayesian Analysis*, 16, 667, doi: [10.1214/20-BA1221](https://doi.org/10.1214/20-BA1221)
- Virtanen, P., Gommers, R., Oliphant, T. E., et al. 2020, *Nature Methods*, 17, 261, doi: [10.1038/s41592-019-0686-2](https://doi.org/10.1038/s41592-019-0686-2)
- Vital, E., van der Marel, R. P., Sohn, S. T., et al. 2025, *HSTPROMO Internal Proper Motion Kinematics of Dwarf Spheroidal Galaxies: II. Velocity Anisotropy and Dark Matter Cusp Slope of Sculptor*, <https://arxiv.org/abs/2508.20711>
- Walker, M. G., & Peñarrubia, J. 2011, *The Astrophysical Journal*, 742, 20, doi: [10.1088/0004-637x/742/1/20](https://doi.org/10.1088/0004-637x/742/1/20)
- Zhu, L., van de Ven, G., Watkins, L. L., & Posti, L. 2016, *MNRAS*, 463, 1117, doi: [10.1093/mnras/stw2081](https://doi.org/10.1093/mnras/stw2081)